Added Resistance in Oblique Waves on a Container Ship Using CFD

Mikkelsen, H.; Shao, Y.; Walther, J. H.

Publication date:
2022

Document Version
Publisher's PDF, also known as Version of record

ADDED RESISTANCE IN OBLIQUE WAVES ON A CONTAINER SHIP USING CFD

H. Mikkelsen[1], Y. Shao[1] and J. H. Walther[1,2]

ABSTRACT

The importance of CFD is increasing in marine hydrodynamics in studying seakeeping and added resistance of ships. While extensive numerical studies have been reported for various ships in head seas in the literature, much fewer CFD studies are found for oblique waves, which in practice is very important in, for instance, estimating required power and maneuverability of ships in realistic sea states. In this paper, the added resistance and motion responses for the KCS container ship in regular waves are studied and validated systematically for two wave headings and six wavelengths using CFD. The ship is free to heave, pitch, and roll. User-defined implementations in the commercial CFD code are made to effectively constrain the surge and yaw. Results of the CFD model are compared with up to three sets of experimental data sets, Potential Flow (PF) and existing CFD results from the literature. In general, the present CFD results show significantly better agreement with the experiments than previously published CFD results. The present study shows that CFD simulations can accurately predict motion responses and added resistance in oblique regular waves. With these results, designers of ship hulls can get an insight of where to focus the optimization work in the pursuit of fuel-efficient vessels.

KEY WORDS

CFD; Added resistance in waves; Oblique waves; Design; Seakeeping.

INTRODUCTION

For the last decades most commercial ship hulls have been designed and optimized for sailing fully loaded with full speed in calm water. Traditionally, the effects of wind and waves have been included by adding a sea margin of 15 percent (Molland et al., 2011) to the required engine power. Over the last 10 years, this single design point approach has started to change by including more draughts and speeds into the design matrix (Psaraftis and Kontovas, 2014). This has narrowed the gap between the conditions ships are design for and the conditions the ships will operate in. However, almost all ship hulls are still designed using a combination of experience, towing tank tests and Computational Fluid Dynamics (CFD), mostly in calm water. The next natural step is to include the influence of interaction with waves into the ship hull design phase. Since almost no ships are constantly sailing in calm water, optimizing the ship hull to realistic sea states in the future has significant potential to reduce fuel costs and emissions. Seakeeping tests of motion responses and added resistance in towing tanks can be expensive, time demanding and dependent on the availability of the tanks. If numerical approaches are verified and validated to become trustworthy, they could be used with confidence in the design phase of new ship hulls. Since numerical simulations only require an available computer and not a large manufactured wooden ship model or a free towing tank slot, ship designers can easily test the seakeeping capabilities of tens or hundreds of ship hulls in the design phase. The use of numerical approaches also makes it possible to study the full-scale ships (Jasak et al., 2018;

[1] Technical University of Denmark, Department of Mechanical Engineering, Nils Koppels Allé, Building 404, 2700 Kgs. Lyngby, Denmark.
[2] Swiss Federal Institute of Technology Zurich, Computational Science & Engineering Laboratory, Clausiusstrasse 33, CH-8092 Switzerland

Niklas and Pruszko, 2019; Mikkelsen and Walther, 2020) and thereby avoid scale effects. The knowledge of a ship's seakeeping properties is also important from both a comfort and safety point of view. Most often, the comfort limit is reached before the motion limit for safety, especially for passenger ships. For non-passenger ships, comfort limits related to ship motions in waves are not as strict. For these ships, the safety can sometimes be the limiting factor, e.g., for container ships, where containers can fall into the sea, if motions become too large. However, the added resistance in waves is important for all ships, since it increases fuel consumption and potentially limits the ship speed.

One of the first studies of added resistance in waves is by Storm-Tejsen et al. (1973), who conducted added resistance experiments of the series 60 ships. Fujii and Takahashi (1975) compared experiments and strip theory simulations on the S175 container ship. Most seakeeping and added resistance research have been focusing on head sea waves. Added resistance in head sea waves using CFD, has been studied intensively by e.g., Sadat-Hosseini et al. (2013), who numerically studied the KRISO Very Large Crude 2 Carrier (KVLCC2). Kim et al. (2017) have also studied the KVLCC2 using both CFD and 3D potential flow theory. Park et al. (2016) studied the added resistance of a tanker in head sea waves at different drafts using the Salvesen-Tuck-Faltinsen (STF) strip theory (Salvesen et al., 1970) and a B-spline based time-domain Rankine panel method (Kim et al., 2011). Simonsen et al. (2013) and Wu et al. (2020) studied the added resistance of the KRISO Container Ship (KCS) in head sea waves both experimentally and using CFD.

Fewer validation studies have been conducted in oblique waves. Studying the ship-wave interaction in oblique waves is important in order to quantify the added power and maneuverability in a realistic sea, where the waves are seldomly uni-directional. A study by Sadat-Hosseini et al. (2015) presented experiments, potential flow, and CFD computations for added resistance for variable headings and wave lengths for the KCS. However, CFD simulations were only conducted for one wavelength. They found that the potential-flow method captures the heave and pitch motions well. However, surge, roll, and added resistance were not well predicted for most cases. In general, the accuracy of the CFD simulations was better. The reason why CFD simulations were only conducted for one wavelength, is that only one wave length was studied at the Tokyo 2015 CFD workshop (Hino et al., 2020). The Tokyo 2015 CFD workshop had a test case, where participants submitted CFD results of motion responses and added resistance for five headings and a single wavelength. Only two participants presented their CFD simulations. The first was Iowa Institute of Hydraulic Research (IIHR) using the CFD code CFDShip-Iowa Sadat-Hosseini et al. (2015). The second was University of Zagreb (UZ) using Naval Hydro Pack (Vukcevic and Jasak, 2016). Both participants showed fair prediction of the motion responses, but the discrepancy of added resistance between the CFD simulations and experiments were up to 100 %.

Considering the increasing popularity of CFD modelling in ship hydrodynamics and its potential capacity to model a more complex phenomenon that an ordinary PF approach cannot handle, e.g., water entry and exit, local wave breaking, viscosities, etc., there is a strong need for dedicated verification and validation studies for ships in waves with various heading and wavelengths.

The aim of the present study is to conduct validation studies of CFD simulations of motions responses and added resistance in oblique waves. The present study conducts CFD simulations of the KCS in two headings and six

wavelengths. The validation is done by comparing the CFD results with experiments from IIHR (Sadat-Hosseini et al., 2015; Sanada et al., 2021) and FORCE Technology (Simonsen et al., 2013).

METHODOLOGY

The present Unsteady Reynolds Averaged Navier-Stokes (URANS) CFD simulations are performed with the commercial CFD-code STAR-CCM+ v.2020.1 from Siemens (2020). STAR-CCM+ discretizes the governing equations using an unstructured finite-volume method. The code is widely used in the marine industry and is well known for its capabilities within marine applications. The CFD model has previously been validated for calm water resistance calculations in both model and full-scale (Mikkelsen et al., 2019; Mikkelsen and Walther, 2020).

KCS and Towing Tank Test

The studied ship is the Kriso Container Ship (KCS). The main particulars of the KCS can be seen in Table 1. The KCS is chosen since both experimental data and the hull geometry is publicly available. The studied wave conditions are shown in Table 2. The present study uses the same ship-fixed coordinate system used by IIHR (Sadat-Hosseini et al., 2015; Sanada et al., 2021) and is seen in Fig. 1. The towing tank tests at IIHR are conducted in a $40\text{m} \times 20\text{m} \times 3\text{m}$ wave basin (Sadat-Hosseini et al., 2015). Unless otherwise mentioned, this same model scale described in Table 1 will be used in all analyses in this paper. The towing tank tests in head sea by FORCE Technology are conducted with a longer ship model with $L_{pp} = 4.37$ m and a $240\text{m} \times 12\text{m} \times 5.5\text{m}$ wave basin.

Table 1: Main particulars

	Symbol	Value
Length between perpendiculars	L_{pp}	2.7 m
Beam	B	0.378 m
Draft	T	0.1268 m
Longitudinal radius of gyration	k_{xx}	$0.39B$
Transverse radius of gyration	k_{yy}	$0.25\ L_{pp}$

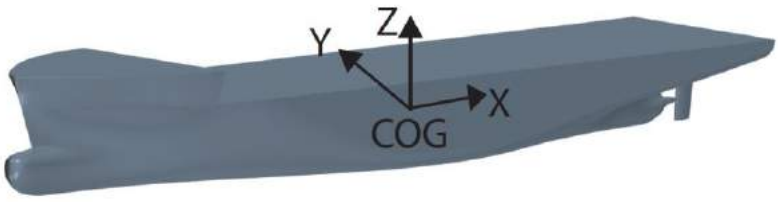

Figure 1. KCS ship geometry and coordinate system.

Table 2: Simulated wave conditions

Wave heading	Wave lengths [-]
Head sea	$\lambda/L = (0.5, 0.75, 1.00, 1.25, 1.50, 2.00)$
Bow sea	$\lambda/L = (0.5, 0.75, 1.00, 1.25, 1.50, 2.00)$

Computational Domain and Wave Generation

The shape of the CFD domain is a rectangular box. The top of the domain is set to a pressure outlet in order to allow the air flow to evolve freely. All vertical sides are velocity inlets. When all vertical sides are velocity inlets and not pressure outlets, the heading of the ship can be allowed to change in future maneuvering simulations. The modelled water depth in the CFD model is 3m, which is the same as that in the model tests. Since the longest wavelength considered in our study is 5.4m, it is not expected that the water depth has any important effects on the seakeeping and added resistance of the ship. Therefore, the bottom of the domain is treated as a velocity inlet.

The total computational domain contains two parts, namely the forcing zone (or relaxation zone) and the solution zone, see Fig. 2 for an illustration. The forcing zone at the outer layer of the computational domain is used to generate the incident regular waves. A smooth-transition function in the form of $cos^2(x)$ is applied within the forcing zone, so that the flow solution is enforced to be the same as the prescribed incident waves at the outer boundaries (the 4 vertical boundaries), while the forcing becomes zero at the end of the forcing zone, i.e. close to the boundary of the solution zoom. The forcing zone also acts as a wave absorbing zone due to the relaxation of the solution towards the targeted incident wave solution at the outer boundaries. In this paper, Stokes fifth-order waves are used as input waves, which are available from the built-in wave module in STAR-CCM+. The steepness of the incident wave is 1.7% in order to match the experimental data provided in (Sadat-Hosseini et al., 2015) and (Sanada et al., 2021).

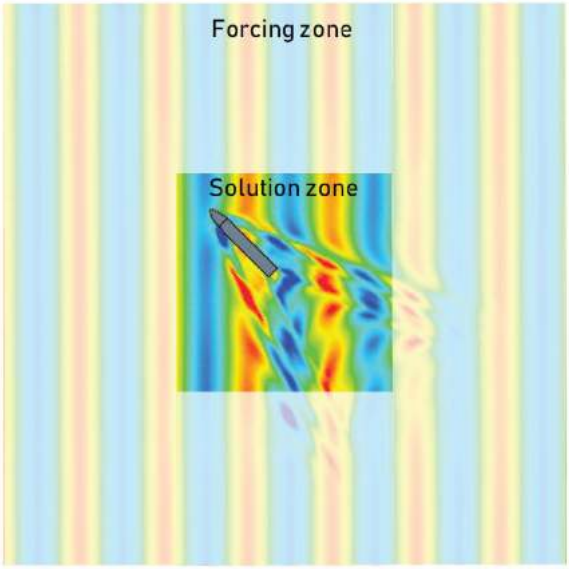

Figure 2. Forcing zone, solution zone and wave elevation for bow quartering sea and $\lambda/L_{pp} = 1$.

The width of the forcing zone is equal to two times the wavelength of the incident wave. The influence of the forcing zone width has been studies in detail. It is found that a forcing zone width of two incident wavelengths is a good compromise between numerical diffusion, wave reflection and computational cost. A forcing zone width of only one incident wavelength caused significant reflection (not shown). The inner volume, where no forcing is applied, is denoted the solution zone. The size of the solution zone is slightly different for each heading because the combination of generated steady Kelvin wave pattern and unsteady diffraction and radiation waves is different for each heading. However, the size of the solution zone is the same for all wavelengths for a given heading. A

size of the solution zone of approximately $3L_{pp} \times 3L_{pp}$ is chosen, so it is enough not to influence the added resistance and seakeeping.

Motions

In the IIHR experiments (Sadat-Hosseini et al., 2015; Sanada et al., 2021), the ship is fixed in z-rotation (yaw) and y-translation (sway). A spring-mass system is used in the experiments in the x-direction (surge), as described by Sadat-Hosseini et al. (2015). However, the surge motions are small (less than $1\%\ L_{pp}$) and for the Tokyo CFD workshop (Hino et al., 2020), which the experiments are made for, it was recommended to constrain the surge in the numerical studies. Therefore, the aim is to make a CFD model, where only the ship is free in z-translation (heave), *y*-rotation (pitch) and *x*-rotation (roll).

In the CFD model, the heave, pitch, and roll motions of the vessel are solved using the Dynamic Fluid Body Interaction (DFBI) Multi Body solver in STAR-CCM+ cf. (Ohmori, 1998; Siemens, 2020) and is applied as a rigid translation and rotation of the overset domain mesh. The DFBI Multi Body solver is chosen for its stability and accuracy. Sway is constrained accurately by the motion solver in STAR-CCM+. However, the DFBI solver in STAR-CCM+ version 2020.1 is found to produce an unacceptable drift in the constrained yaw. Besides the drift, it is found that constraining the yaw motion by the built-in motion module in STAR-CCM+ makes the roll response non-physical. Therefore, the surge and yaw motions are constrained using implementations by the authors. The surge motion is constrained by applying a concentrated *x*-force at each time step in the center of mass equal to the integrated shear and pressure forces acting on the hull with opposite sign. With this implementation, the speed of the ship never deviates more than 0.1% from the target ship speed. Since the integrated *x*-force is calculated each time step, the implementation allows the ship speed to be non-constant in future studies of, for instance, maneuvering simulations in waves and self-propulsion simulations in waves. The yaw motion is constrained by applying a concentrated z-moment and a torsional spring around the z-axis of the ship. The magnitude of the applied concentrated z-moment is equal to the integrated z-moment of the ship with opposite sign. The torsional spring constant is set to $20\mathrm{kNm/deg}$ in order to ensure a small yaw angle and a natural yaw frequency far from the natural frequencies of the motions and incident waves. The magnitude of the concentrated z-moment is approximately 50 times larger than the *z*-moment from the torsional spring. With this implementation, the simulated yaw angle never exceeds 0.01 deg and it is found not to influence the other motions.

Post-Processing of the Results

The main output from the simulations are time histories of heave (*Z*), pitch (θ), roll (φ) and total resistance (R). The resistance is the integrated shear stress and pressure on the hull in the *x*-direction. An example of a resistance time history is shown in Fig. 3. From an instant, where the solution $(s(t))$ has periodically steady outputs, an integer number of encounter periods T_e are fitted to a 4-term Fourier series:

$$s(t) = a_0 + a_1 \cos(\omega_1 t) + b_1 \sin(\omega_1 t) + \cdots + a_4 \cos(\omega_4 t) + b_4 \sin(\omega_4 t) \quad [1]$$

where $\omega_k = 2\pi\ f_e\ k$, and f_e is the encounter frequency.

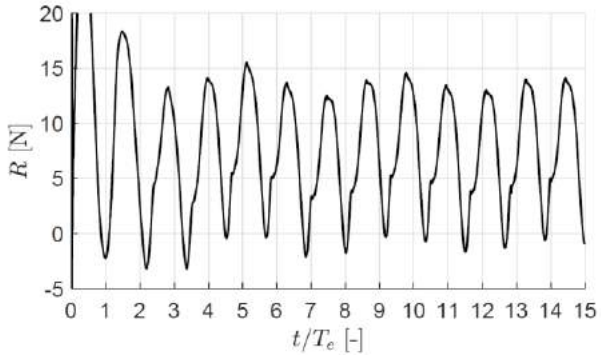

Figure 3. Time history of the measured resistance (R) at bow quartering sea and $\lambda/L_{pp} = 1$ as function of the time non-dimensionalized by with the encounter period (T_e).

Each fit is visually inspected to ensure that the fit is representable of the time history and that the fitting window does not start before the time history has stabilized. For the time history shown in Fig. 3, the fit only uses the time history for $t/T_e = 9 - 15$. Based on the Fourier coefficients from these fits, the amplitudes (A_k) for heave, pitch, roll, and resistance are calculated using:

$$A_k = \sqrt{a_k^2 + b_k^2} \quad [2]$$

where k is the Fourier term.

The same procedure is used in the Tokyo workshop (Hino et al., 2020) allowing for direct comparison. The present study only focuses on the added resistance and the first amplitude of heave (Z_1), pitch (θ_1), roll (ϕ_1). The added resistance (σ_{aw}) is defined as

$$\sigma_{aw} = \frac{R_0 - R_{CW}}{\frac{\rho g A^2 B^2}{L_{pp}}} \quad [3]$$

where R_0 is the zero-th amplitude (mean) resistance using Equation 1 and R_{CW} is the calm water resistance.

For the validation, the amplitudes are non-dimensionalized with the incident wave amplitude that actually reaches the ship and not the target wave amplitude, which is specified at the domain boundaries. The added resistance will also be calculated using the actual wave amplitude.

RESULTS AND DISCUSSION

The present CFD model is validated for each of the two studied headings in the following two subsections. The present CFD results are compared with up to three sets of Experimental Fluid Dynamics (EFD) data. For all headings, two set of experimental data are from IIHR by Sadat-Hosseini et al. (2015) and Sanada et al. (2021). The study by Sanada et al. (2021) also presents a calculated standard deviation for the $\lambda/L_{pp} = 1$ waves. These standard deviations are included as error bars in Fig. 4 and 5. In head sea, the results from FORCE Technology by Simonsen et al. (2013) are also included in the comparison as (FORCE). Furthermore, the present CFD results are compared with potential flow (PF) results by Sadat-Hosseini et al. (2015) who used the 3D PF code FATIMA (Bunnik, 1999). At the Tokyo CFD workshop in 2015, only two participants submitted their CFD results for the

case with motion responses and added resistance in oblique waves. The first participant is IIHR using the CFD code CFDShip-Iowa (Sadat-Hosseini et al. 2015). The second participant is University of Zagreb (UZ) using Naval Hydro Pack (Vukcevic and Jasak, 2016). Translatory and rotational motion responses are non-dimensionalized by the actual wave amplitude (A) and wave steepness (kA) respectively, where $k = \frac{2\pi}{\lambda}$. The added resistance is calculated using Equation 3.

Head sea

The comparison of the present CFD results, previously reported CFD and PF results, and three sets of experimental data for head sea can be seen in Fig. 4. For this heading, the agreement between the three experimental data sets is good. Both the present CFD, UZ CFD and PF motions responses agree very well with the experiments. In general, the present CFD results show slightly better agreement in motion responses than the PF results, especially for the longer waves. The encounter frequency of the $\lambda/L_{pp} = 1.25$ wave is very close to the natural heave and pitch frequencies causing resonance. The CFD by IIHR and the PF results overestimates the added resistance near the resonance area by approximately 45%. However, the added resistance estimated by the present CFD model is within the standard deviation of the experiments by Sanada et al. (2021).

Bow quartering sea

Fig. 4 shows the comparison of the present CFD results, previously reported CFD and PF results, and two sets of experimental data for bow quartering sea. The heave responses shown in Fig. 5a, predicted by both the present CFD and PF agree very well with the experiments. The largest deviation is observed for the longest wave. However, the deviation is still smaller than the difference between the two sets of experiments. For the pitch response, shown in Fig. 5b, both the present CFD and PF agree well with the experiments for the two shortest waves. For the longer waves, both the PF and the present CFD results approach an asymptotic limit. The PF agrees excellently with the pitch found in the EFD by Sadat-Hosseini et al. (2015) for all wavelengths and approaches an asymptotic value very similar to the value found by the experiments by Sadat-Hosseini et al. (2015) at $\lambda/L_{pp} = 2.0$. The present CFD approaches a value similar to the value found in the experiments by Sanada et al. (2021) at $\lambda/L_{pp} = 2.0$. The CFD by UZ predicts the heave and pitch responses well, whereas the CFD by IIHR overestimates the heave and pitch responses by approximately 10%. The roll responses found in the experiments are much larger than any of the numerical methods as seen in Fig. 5c. The roll responses predicted by the PF and all three CFD approaches agree well with each other, but not with the experiments. Even the smallest encounter frequency of the studied waves in bow quartering sea is 0.72 Hz. This is more than double the natural roll period (0.33 Hz) with forward speed. It is not clear why the experimental roll responses are about one order of magnitude higher than numerical results. This needs more dedicated experimental studies in the future and is out of the scope of the present study. When the wavelength is increased, the encounter frequency is decreasing for the bow quartering sea. Therefore, it is expected that the roll responses should only increase slowly while the wavelength is getting larger, and the encounter frequency becomes closer to the natural roll frequency. This is the behavior of all the numerical results in Fig. 5c. In general, both the PF and the present CFD overestimates the added resistance at the shorter waves and underestimates the added resistance at the longer waves as seen in Fig. 5d.

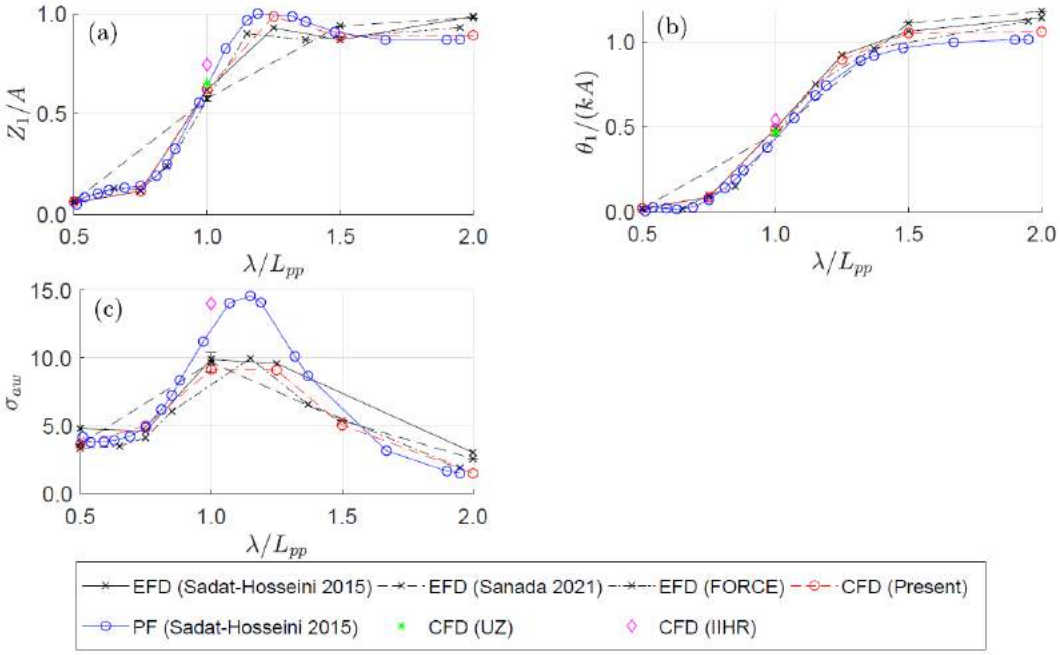

Figure 4. Comparison of results for head sea as a function of non-dimensional wavelength (λ/L_{pp}). (a) Heave, 1st amplitude (Z_1); (b) Pitch, 1st amplitude (θ_1); (c) Added resistance (σ_{aw}).

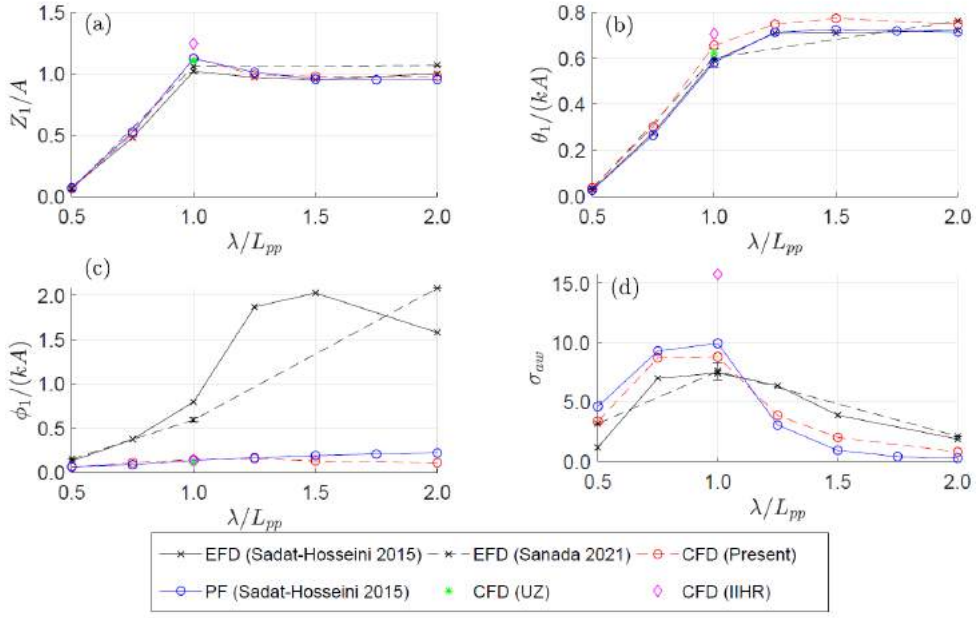

Figure 5. Comparison of results for bow quartering sea as a function of non-dimensional wavelength (λ/L_{pp}). (a) Heave, 1st amplitude (Z_1); (b) Pitch, 1st amplitude (θ_1); (c) Added resistance (σ_{aw}).

However, the added resistance from the present CFD is closer to the experiments for all wavelengths than the PF results. For the $\lambda/L_{pp} = 1.0$ wave, the CFD by IIHR overestimates the added resistance by approximately 100%, whereas the present CFD overestimates the added resistance by approximately 18%. The standard deviation of the experimental added resistance by Sanada et al. (2021) is 10.7% at this wave.

CONCLUSION

This study presents a validation of seakeeping responses and added resistance of the KCS container ship in regular oblique waves by using CFD. The surge and yaw motions are constrained by user-implementations in the commercial software, which consist of additions of springs and concentrated forces/moment to cancel the fluid forces and moments. For each test case, the added resistance as well as the heave, pitch, and roll response are compared with previously reported potential flow and CFD results and up to three sets of experimental data. Due to the loss of incident wave amplitude caused by numerical diffusion, the motion and added resistance results are non-dimensionalized based on the actual incident wave amplitude obtained from separate runs in an empty wave tank, where similar spatial and temporal discretization is used.

In most cases the discrepancy between the experiments and the present CFD results are within the uncertainty of the experiments. In general, both the previously reported potential flow calculations and present CFD simulations predict the motion responses well. However, the added resistance predicted by the present CFD model is in better agreement with the experiments, than the previously reported potential flow results. Furthermore, the present CFD results in general show significantly better agreement with the experiments than previously published CFD results. The tendencies in the results of the present CFD model matches very well the expected behavior regarding the natural motion frequencies of the ship. The study has shown that CFD simulations accurately can predict motion responses and added resistance in oblique regular waves.

ACKNOWLEDGEMENT

The research is supported by the Danish Maritime Fund under grant 2018-11, whose support is greatly appreciated.

REFERENCES

Bunnik, T. H. J. (1999). “Seakeeping calculations for ships, taking into account the non-linear steady waves”. PhD thesis, Delft University of Technology.

Fujii, H. and Takahashi, T. (1975). “Experimental study on the resistance increase of a large full ship in regular oblique waves", Numerical ship hydrodynamics: An assessment of the Tokyo 2015 workshop. Springer-Verlag.

Jasak, H., Vukčević, V., Gatin, I., and Lalović, I. (2018). “CFD validation and grid sensitivity studies of full scale ship self propulsion”. Int. J. Nav. Archit. Ocean Eng., 11(1):33–43.

Kim, Y., Kim, K.-H., Kim, J.-H., Kim, T., Seo, M.-G., and Kim, Y. (2011). “Time-domain analysis of nonlinear motion responses and structural loads on ships and offshore structures: development of WISH programs”. Int. J. Nav. Archit. Ocean Eng., 3(1):37–52.

Kim, M., Hizir, O., Turan, O., and Incecik, A. (2017). “Numerical studies on added resistance and motions of KVLCC2 in head seas for various ship speeds”. Ocean Engng., 140(May):466–476.

Mikkelsen, H., Steffensen, M. L., Ciortan, C., and Walther, J. H. (2019). “Ship scale validation of CFD model of self-propelled ship”. In MARINE 2019 Computational Methods in Marine Engineering VIII, pages 718–729.

Mikkelsen, H. and Walther, J. H. (2020). “Effect of roughness in full-scale validation of a CFD model of self-propelled ships”. Appl. Ocean Research, 99:1–14.

Molland, A., Turnock, S., and Hudson, D. (2011). “Ship resistance and propulsion”. Cambridge University Press.

Niklas, K. and Pruszko, H. (2019). “Full-scale CFD simulations for the determination of ship resistance as a rational, alternative method to towing tank experiments”. Ocean Engng., 190:1–13.

Ohmori, T. (1998). “Finite-volume simulation of flows about a ship in maneuvering motion”. J. Mar. Sci. Tech., 3(2):82–93.

Park, D. M., Kim, Y., Seo, M. G., and Lee, J. (2016). “Study on added resistance of a tanker in head waves at different drafts”. Ocean Engng., 111:569–581.

Psaraftis, H. N. and Kontovas, C. A. (2014). “Ship speed optimization: Concepts, models and combined speed-routing scenarios”. Transp. Res. Part C Emerg. Technol., 44:52–69.

Sadat-Hosseini, H., Wu, P. C., Carrica, P. M., Kim, H., Toda, Y., and Stern, F. (2013). “CFD verification and validation of added resistance and motions of KVLCC2 with fixed and free surge in short and long head waves”. Ocean Engng., 59:240–273.

Sadat-Hosseini, H., Toxopeus, S., Kim, D. H., Sanada, Y., Stocker, M., Otzen, J. F., Toda, Y., and Stern, F. (2015). “Experiments and computations for KCS added resistance for variable heading”. In 5th World Maritime Technology Conference, pages 1–15.

Salvesen, N., Tuck, E., and Faltinsen, O. (1970). “Ship motions and sea loads”. Trans. - Soc. Nav. Archit. Mar. Eng., 78:250–287.

Sanada, Y., Simonsen, C., Otzen, J., Sadat-Hosseini, H., Toda, Y., and Stern, F. (2021). “Experimental data for KCS added resistance and ONRT free running course keeping/speed loss in head and oblique waves”, volume 94. Springer-Verlag.

Siemens (2020). STAR-CCM+ user guide, version 2020.1.

Simonsen, C. D., Otzen, J. F., Joncquez, S., and Stern, F. (2013). ”EFD and CFD for KCS heaving and pitching in regular head waves”. J. Mar. Sci. Tech., 18:435–459.

Storm-Tejsen, J., Yeh, H. Y. H., and Moran, D. D. (1973). “Added resistance in waves”. Trans. - Soc. Nav. Archit. Mar. Eng., 81:250–279.

Vukčević, V. and Jasak, H. (2016). “Validation and verification of decomposition model based on embedded free surface method for oblique wave seakeeping simulations”. In Tokyo 2015: A Workshop on CFD in Ship Hydrodynamics, pages 495–502.

Wu, P.-C., Hossain, M. A., Kawakami, N., Tamaki, K., Kyaw, H. A., Matsumoto, A., and Toda, Y. (2020). “EFD and CFD study of forces, ship motions, and flow field for KRISO container chip model in waves”. J. Ship. Res., 64(1):61–80.

Towards hydrodynamic modelling of ship-to-ship LNG bunkering in waves with focus on gap resonance

Y. F. Ding[1], J. H. Walther [1, 2] and Y. L. Shao[1]

ABSTRACT

Ship-to-ship bunkering of liquid fuel, e.g., LNG, outside the port can be a flexible and cost-efficient solution without having to upgrade the infrastructures at the port. The occurrence of fluid resonance in the narrow gap between side-by-side receiving vessel and bunkering vessel under wave actions may greatly influence the dynamic responses of the vessels through hydrodynamic interaction. The proximity of marine structures can generate drastic wave elevation in the narrow gap, which may reduce the operational time window of the bunkering and even risk the safety of the crew. In this paper, the fluid resonance inside the gap between two non-identical ship cross-sections in side-by-side configuration is studied under various wave conditions. The bunkering scenario that a larger cross-section on the upstream is fixed while a small cross-section free to heave in the downstream is considered as more realistic. A numerical wave tank is set up based on the commercial CFD package STAR-CCM+. The unsteady Reynolds averaged Navier-Stokes turbulence model is required to consider viscous dissipation. The volume of fluid method is applied to capture the position of the free surface, and regular waves are generated and absorbed using forcing zones at upstream and downstream boundaries, respectively. The overset meshing technique is employed near the downstream section to enable the heave motion. The heave response of the downstream section and its effect on the linear and nonlinear harmonics of wave elevation and resonant frequency inside the gap are investigated and compared with the fixed-sections scenario. It can be concluded that the heave motion reduces the gap resonance to a large extent by modulating the frequency of wave elevation inside the gap, thus avoiding the occurrence of second-order excitation.

KEY WORDS

Gap resonance; Ship-to-ship LNG bunkering; Harmonic analysis; Free heave motion; STAR-CCM+.

INTRODUCTION

Recently, ship-to-ship bunkering has become a more efficient and safe way to fuel the LNG-fueled vessels outside the port. During the bunkering operations, fluid resonance inside the gap between the side-by-side receiving vessel and bunkering vessel may elevate the water surface within the gap to a large extent and influence the dynamic responses of the vessels due to hydrodynamic interaction. One of the relevant and important phenomena is referred to as piston-mode gap resonance in the literature, which is a key hydrodynamic issue that needs a thorough and deep understanding of the underlying physics. Large wave elevation due to the gap resonance may also lead to wave impacts on the soft hoses which are typically used to transfer liquid LNG between the two vessels.

Physical experiment is a direct approach to explore this problem (Kristiansen and Faltinsen 2008, 2010; Faltinsen, et al. 2011; Tan, et al. 2014). Saitoh et al. (2006) conducted laboratory experiments to understand the characteristics of fluid resonance in the gap between two fixed barges exposed to waves. Perić and Swan (2015) used experiments to characterize both the amplitude and nature of the excitation within the gap. Experiments were also carried out by Ning et al. (2018) to investigate the wave response in the gap between two barges of different draughts in incident waves.

Early numerical studies towards fluid resonance in a confined region with the presence of a free surface started with the theoretical investigation based on the linear potential-flow theory (Miao, et al. 2000; Iwata, et al. 2007; Zhu, et al. 2008).

[1] Department of Mechanical Engineering, Technical University of Denmark, 2800 Kgs. Lyngby, Denmark
[2] Computational Science and Engineering Laboratory, ETH Zürich, CH-8092 Zürich, Switzerland

Molin (2001) considered rectangular moonpools of large horizontal dimensions and determined the natural modes for the oscillation of the inner free surfaces in both two and three dimensions. Improved potential-flow methods with viscous corrections were applied to avoid non-physically large wave elevation within the gap at the resonance (Tan, et al. 2014; Ning, et al. 2015a, 2015b; Zhao, et al. 2018; Tan, et al. 2019). Based on both the viscous-flow model and the potential-flow model with the introduction of artificial damping term, Lu et al. (2011) presented two-dimensional (2D) numerical results of the wave loads on multiple floating bodies in close proximity and their dependences on the wave frequency, gap width, body draft, body breadth, and the number of bodies. However, they pointed out that the artificial damping has to be calibrated by model tests or Computational Fluid Dynamics (CFD) simulations in order to achieve better prediction, which may lose its advantage and limit the application of the potential-flow models to a large extent.

With the development of the capacity of modern computers to run large-scale computations, CFD methods based on Navier-Stokes equations have become a popular alternative to deal with the gap resonance problem (Lu, et al. 2010; Chua, et al. 2018; Jiang and Bai 2020). Moradi et al. (2016) reported that the water depth, body draft, and the ratio between water depth and body draft are the key factors that influence the resonant responses. It was also found that the potential-flow models not only overpredict the resonant wave heights but also fail to predict the variation trends of the resonant wave height as function of water depth. In the work of Jiang et al. (2019), piston-mode wave resonance between a ship section and a bottom-mounted terminal was studied, where it is also confirmed that the effects of fluid viscosity and the vorticity increase significantly with the increase of incident wave amplitudes. Some numerical investigations were also carried out by Gao et al. (2019, 2020a, 2020b) to simulate transient resonant motions of the free surface inside a narrow gap under various configurations and wave conditions.

As we can see from the previous studies, the focuses of most existing studies are on the fixed structures (Sun, et al. 2010; Moradi, et al. 2015; Gao, et al. 2019, 2020a, 2020b; Jiang, et al. 2021a, 2021b). In practice, floating marine structures are free to move in certain directions although they may be constrained in other degrees of freedom. To date, only few studies considered the floating structure with certain degrees of freedom of motion (Li and Zhang 2016; Li 2019; Lu, et al. 2020). These studies simulated the coupled motions of two structures and applied the potential-flow models, while the relevance to practical ship-to-ship bunkering operations is not clear. Gao et al. (2021) studied the influence of the free-heave motion of an upstream box on the gap resonance under wave actions while the downstream box remains fixed. However, in practical ship-to-ship bunkering operations, the two vessels are typically very different in size, and, naturally, the small bunkering vessel will be situated behind the larger receiving vessel thus avoiding violent relative motion between them. Therefore, the present work focuses on the gap resonance formed by two non-identical square cross-sections under wave actions. The larger upstream section remains fixed and the smaller downstream section is free to heave.

The remainder of this paper is organized as follows: the mathematical formulation of the numerical model, the applied numerical schemes and solvers are introduced, followed by the establishment of the 2D numerical wave flume. After that, two validation studies are presented, including two fixed barges and a single barge free to heave. Finally, numerical results for two non-identical barges, i.e., a fixed upstream barge and a downstream barge free to heave, are presented.

NUMERICAL MODEL

The Unsteady Reynolds Averaged Navier-Stokes (URANS) turbulence model is applied to consider viscous dissipation and the Volume of Fluid (VOF) implementation is selected to capture the free surface. The motion of the heaving section is realized by employing the overset meshing technique. For more implementations on the scheme and solver regarding the numerical model, interested readers are referred to the book by Ferziger et al. (2002) or the STAR-CCM+ user guide.

Governing Equations

The VOF multiphase model in STAR-CCM+ is applied to predict the distribution and the movement of the interface between the air and water phases, in which mass conservation equation and momentum equation can be expressed as:

$$\frac{d}{dt}\int_V \rho dV + \int_S \rho(\boldsymbol{v}-\boldsymbol{v}_g)\cdot\boldsymbol{n}dS = 0 \quad [1]$$

$$\frac{d}{dt}\int_V \rho u_i dV + \int_S \rho u_i(\boldsymbol{v}-\boldsymbol{v}_g)\cdot\boldsymbol{n}dS = \int_S (\tau_{ij}\boldsymbol{i}_j - p\boldsymbol{i}_i)\cdot\boldsymbol{n}dS + \int_V \rho\boldsymbol{g}\boldsymbol{i}_i dV \quad [2]$$

where V is the control volume bounded by the closed surface S; $\boldsymbol{v}$ and $\boldsymbol{v}_g$ are the velocity vectors of the fluid with the Cartesian components u_i and of the grid, respectively; $\boldsymbol{n}$ is the unit vector normal to S and pointing outwards; t represents the time; p is the pressure and ρ is the fluid density; $\boldsymbol{i}_i$ and $\boldsymbol{i}_j$ are the unit vectors in direction x_i and x_j, respectively; $\boldsymbol{g}$ is the gravity vector; τ_{ij} are the components of the viscous stress tensor.

The volume fraction in this method is defined as:

$$\alpha = \begin{cases} 0, & \text{in air} \\ 0 < \alpha < 1, & \text{at the surface} \\ 1, & \text{in water} \end{cases} \quad [3]$$

Then the spatial variation of any fluid property f (e.g., the density ρ, and the dynamic viscosity μ) can be represented as a weight of α:

$$f = \alpha f_{water} + (1-\alpha) f_{air} \quad [4]$$

in which, the subscript "water" and "air" denote the property of the corresponding phase, respectively.

The governing equation of volume fraction is:

$$\frac{d}{dt}\int_V \alpha dV + \int_S \alpha(\boldsymbol{v} - \boldsymbol{v}_g)\cdot \boldsymbol{n} dS = 0 \quad [5]$$

Here, α is the volume fraction of water. In this study, $\alpha = 0.5$ is adopted to capture the interface between the two phases.

Body and Mesh Motions

The Dynamic Fluid Body Interaction (DFBI) module in STAR-CCM+ is employed to simulate the motion response of the ship section exposed to incident regular waves. In this work, only translatory motion in heave will be considered and solved based on Newton's second law.

The overset meshing technique is coupled with the DFBI module to update the mesh position around the heaving section. Meshes in the overset region move rigidly with the motion of the section, where the solution is coupled with the flow domain (the background region) by linearly interpolating donor-cell values to provide data for acceptor cells.

Boundary Conditions and Numerical Implementations

The wave is generated by prescribing the volume fractions and the velocities according to Fenton's 5th-order Stokes theory at both the inlet and outlet boundaries ($x = -L/2$ and $x = L/2$). Here L denotes the total length of the numerical wave flume. To minimize the undesired wave reflection for long-duration simulations, wave forcing is applied at the inlet and outlet boundaries to enforce the solution of the Navier-Stokes equations towards the prescribed nonlinear wave solution (Kim, et al. 2012). The no-slip boundary condition is imposed on the fixed section and the seabed, and the overset mesh is prescribed on the surfaces of the overset region that moves with the heaving section. The top boundary of the domain is defined as a pressure outlet by prescribing the hydrostatic pressure and the volume fractions of both phases (see Figure 1). The simulations are run in a quasi-2D manner with only one layer of cells in the transverse direction and symmetry boundary conditions are applied on the side-walls of the wave flume. Numerical simulations start from the still-water state with predefined initial conditions of the velocity and hydrostatic pressure of the incident wave.

The governing equations 1, 2 and 5 are solved for each cell based on the finite volume method, with all integrals approximated by the midpoint rule. The VOF method is used to account for the two fluid phases with the setup of angle factor in the High Resolution Interface Capturing scheme (HRIC) to eliminate wiggles on the free surface (Muzaferija and Perić 1999). The standard low-Re k-ε turbulence model with all-y+ wall treatment is applied to prevent excessive growth of turbulent viscosity in the free-surface zone (Perić 2018). The interpolation of variables from cell centre to face centre and numerical differentiation are performed using linear functions (second-order accuracy). The applied time-integration scheme is also of second order. The resulting coupled system of equations is then linearized and solved by the iterative implicit unsteady segregated solver in STAR-CCM+, using a multigrid method. Eight outer iterations are performed in each time step, which consists of solving the governing equations for the velocity components, the pressure-correction equation (using the SIMPLE method), and the transport equations for the volume fraction of water, as well as the turbulent kinetic energy k and the turbulent dissipation rate ε. In addition, the time step is adaptive to satisfy the Courant-Friedrichs-Lewy (CFL) condition on the free surface, that is, $\Delta t \leq C_r \Delta x / v_r$. Here, Δx and v_r are the mesh size and relative velocity of the fluid to the mesh, respectively. To guarantee the accuracy and stability of the results, the maximum convective Courant number C_r on the free surface is set to around 0.1 in all simulations.

NUMERICAL WAVE FLUME

The 2D numerical wave flume is established, which is shown in Figure 1. The height of the wave flume is three times the height H_1 of the larger section and its length is around 9λ, where λ is the incident wavelength. To achieve quasi-2D simulations, only one grid cell is applied along the width of the flume, whose size is set as $W = 0.08H_1$. The origin of the Cartesian coordinate system is set on the still wave line (SWL) and at the middle of the wave flume, with wave propagating along the x-axis and elevating along the z-axis. Two non-identical square sections are located at the centre of the wave flume with a water depth of $h = H_1$ and a gap width of $B_g = 0.1B_1$. The larger upstream section (hereafter denoted as section A) is fixed, which has the height H_1 and breadth B_1 and a draft of $d_1 = 0.5H_1$. The smaller downstream section (hereafter section B) is free to heave with the side width of $H_2 = B_2 = 0.6H_1(B_1)$ and the draft of $d_2 = 0.3H_1$.

To the best of the authors' knowledge, no model-test data for non-identical sections are available in the literature, thus we will use the two identical sections which have been experimentally studied by Saitoh et al. (2006) to validate our setup in the numerical model. For simplicity, the system with two identical fixed boxes will be referred as "*fixed system*" later in this paper, and the other non-identical system studied here with a freely-heaving section is named "*heave system*".

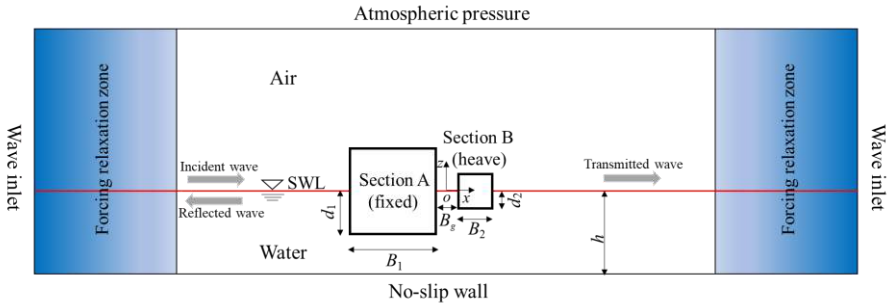

Figure 1: Sketch of the 2D numerical wave flume with two non-identical sections in the middle.

Two Stokes waves (hereafter called wave A and wave B) with equal wave height $H_0 = 0.048H_1$ but different wavelengths $\lambda_A = 4.044B_1$ and $\lambda_B = 9.92B_1$ are considered as incident waves in the numerical analysis. The frequency of wave A corresponds to the natural frequency of the liquid in the gap (the resonant frequency) of the *fixed system*, while the frequency of wave B is half this resonant frequency. Two relaxation zones, whose lengths are twice the wavelengths of the incident regular waves, are applied at the inlet and outlet boundaries respectively to absorb the reflected and transmitted waves.

Trimmed mesh is adopted in the entire domain and a typical mesh configuration is displayed in Figure 2, with finer resolution near the free surface and inside the narrow gap. Near the free surface, the amount of meshes along the vertical z direction is 20 per wave height for all the studied cases and the mesh size along the horizontal x direction is designed to keep a constant aspect ratio $\Delta x/\Delta z = 8$, which was determined based on careful tests to produce high-quality incident waves (details not shown here). The meshes are also refined close to the sections in both phases to better resolve the flow due to the motion of section B and the flow separation around the sharp corners of both sections. The same mesh refinement is supposed to be employed in the overset region with adequate prism layers at the interface to achieve the data interpolation between cells.

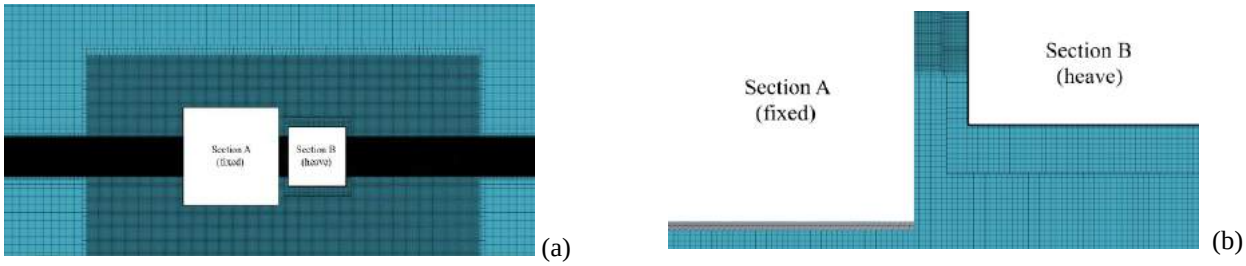

(a) (b)

Figure 2: Mesh configuration in the computational domain: (a) around the sections; (b) close to the gap.

VALIDATION

The present numerical model will be validated by two cases: (I) a *fixed system* with two identical sections and 5 different gap widths; (II) a single section free to heave in waves with 9 different wavenumbers. In the first case, the numerical results of free-surface elevation in the narrow gap obtained by using the computational setup described in the previous section will be compared with the existing experimental data (Saitoh et al. 2006). In the second case, the heave motion of the floating section will be compared with the experimental measurement by Rodríguez and Spinneken (2016).

Free Surface Amplification (Case I)

The simulated non-dimensional wave height amplifications in the gap of various widths B_g for the *fixed system* with incident wave height $H_0 = 0.048H_1$ and non-dimensional water depth $kh = 2.476$ are presented in Figure 3. Here k and h are the wavenumber and water depth, respectively. It has to be noted that the draft of both sections is $d/H_1 = 0.31$ in this validation study. H_g represents the free surface elevation within the gap and B_g is the gap width. It can be seen that the present results correspond well with the experimental data except for a small underestimation for the gap with a width of $0.06B_1$.

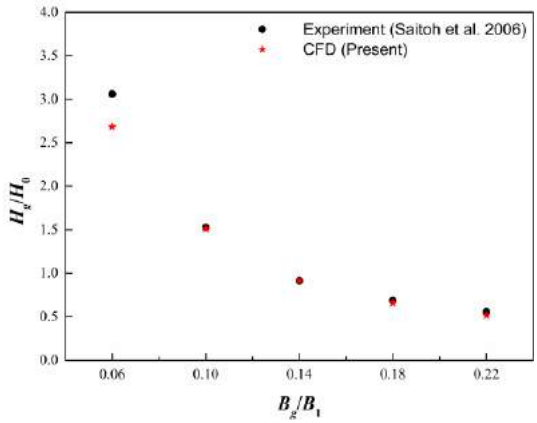

Figure 3: Amplifications of wave elevation (H_g/H_0) in the gap of various widths B_g for the *fixed system*.

Heave Amplitude (Case II)

Rodríguez and Spinneken (2016) carried out physical experiments in a 2D wave flume to investigate the free heave motion of a single rectangular box under regular waves. The wave tank is 63 m long, 2.79 m wide, and has a water depth of 1.25 m. A rectangular box is located at $x = 29$ m while the incident wave is generated from $x = 0$ m. A gap width of 0.015 m is set between the box surface and the side boundaries of the tank to approximate 2D flow condition. The box has a breadth of 0.5 m and a draft of 0.25 m. Stokes waves with the steepness $kA_0 = 0.05$ and different wavenumbers k are considered to validate the present numerical model. Here A_0 denotes the incident wave amplitude. The numerical wave flume adopted (not shown here) is similar to that in Figure 1 except for a different water depth and that a single box in the middle of the wave flume is studied in this validation case. The length of the wave tank is not exactly the same as that in the experiment due to the application of the forcing zones at both the inlet and outlet boundaries. Figure 4 shows the normalized heave motion amplitude of the floating box versus the non-dimensional wavenumber. It is observed that the numerical results correspond well with the experimental data except for some underestimation near the resonance.

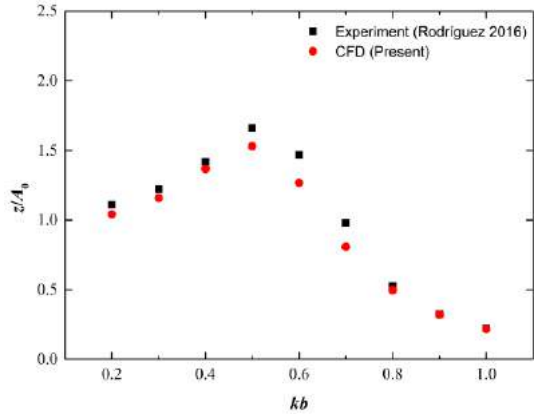

Figure 4: Non-dimensional heave amplitudes (z/A_0) of a free-heaving box under incoming Stokes waves.

RESULTS AND ANALYSIS

To study the effect of the heave motion of downstream section B on the gap resonance, the free surface elevation in the narrow gap is monitored for the *heave system* under the action of incident waves with different wavelengths. Then the Fast Fourier Transform (FFT) method is applied to obtain the harmonics of the responses. Next, the time series of the heave displacement of section B is measured, and its relationship with the vertical force acting on section B is discussed. The harmonic analysis is subsequently carried out for the heave displacement and the results are discussed. Finally, the

flow field of wave A (wave frequency equals to gap-resonant frequency) is demonstrated in the vicinity of the gap to understand the physics of this phenomenon.

Free Surface Elevations

Overall Amplifications

The non-dimensional time histories of free surface elevation inside the gap for the *heave system* exposed to two Stokes waves (wave A and wave B) are shown in Figure 5. The corresponding results for the *fixed system* and the incident-wave elevation are also included for comparison. It is observed that the wave elevations in the gap for the *heave system* under both waves are smaller than those for the *fixed system*, and are also smaller than the incident wave amplitudes. Large wave amplitude appears in the gap for the *fixed system* when the wave frequency coincides with the natural frequency of the water bulk within the gap, which demonstrates the occurrence of the gap resonance and the corresponding Response Amplitude Operator (RAO), namely the ratio of amplitude of free surface elevation in the narrow gap to the height of the incident wave, can reach up to 4.6. For incident wave B, the elevation decreases to around 1.5 times the incident wave height for the *fixed system*. It should be noted that the second-order component presents as a result of nonlinear wave-wave and wave-structure interactions in wave case B (wave frequency equals to half-resonant frequency). When the incident wave frequency is close to half the resonant frequency, the second-order wave loads can stimulate the resonant gap response. The wave elevations in the narrow gap for the *heave system* do not show similar trends as those for the *fixed system*. The heave motion of section B absorbs the energy in the gap and modulates the resonant frequency to some extent.

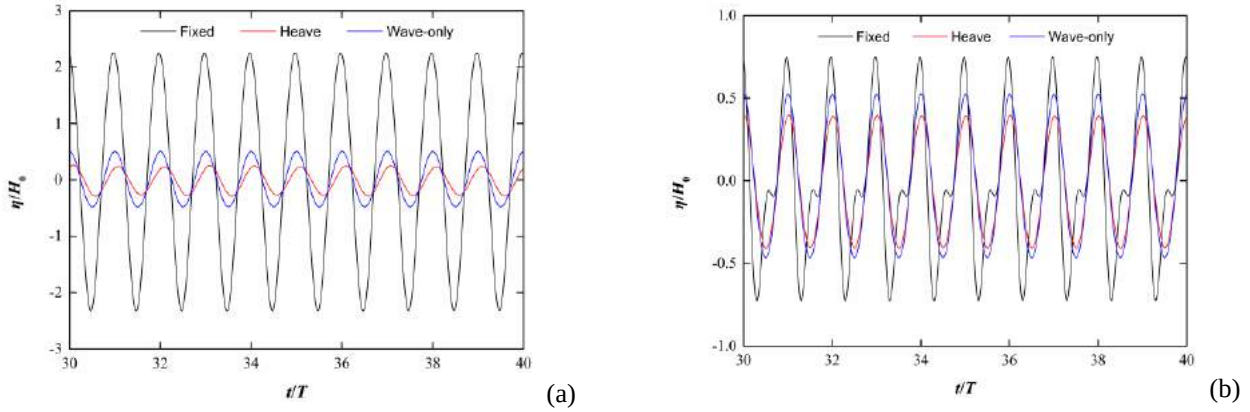

Figure 5: Time history of the free surface elevation in the gap (η/H_0) for the *fixed system* and *heave system* under different incident wavelengths: (a) Stokes wave A (resonance); (b) Stokes wave B (half-resonance).

Harmonic Analysis

Harmonic analysis is performed to understand the contribution of each frequency component. Figure 6 presents the first three orders of normalized amplitudes of the free-surface elevation in the gap for both the *fixed system* and *heave system* under different incident waves, and the amplitudes of the harmonics are listed in Table 1. It can be seen that the first-harmonic component of wave elevation in the gap is excited in the *fixed system* at the resonance, while the first-harmonic component for the *heave system* remains smaller than the incident wave amplitude. A rather small second-harmonic component can be observed for the *heave system*. When the incident wave frequency is half the resonant frequency, the second-harmonic component is excited in the *fixed system*, and its amplitude can take up 42.4% of the first-harmonic component while the first-harmonic component drops back to a bit larger than that of the incident wave, which is consistent with the conclusion in the previous time-domain result. The second-harmonic component of wave elevation is not stimulated by the incident wave for the *heave system*. This is due to the existence of heave motion of section B, which modulates the frequency of the free surface variation inside the gap and averts the occurrence of second-order excitation.

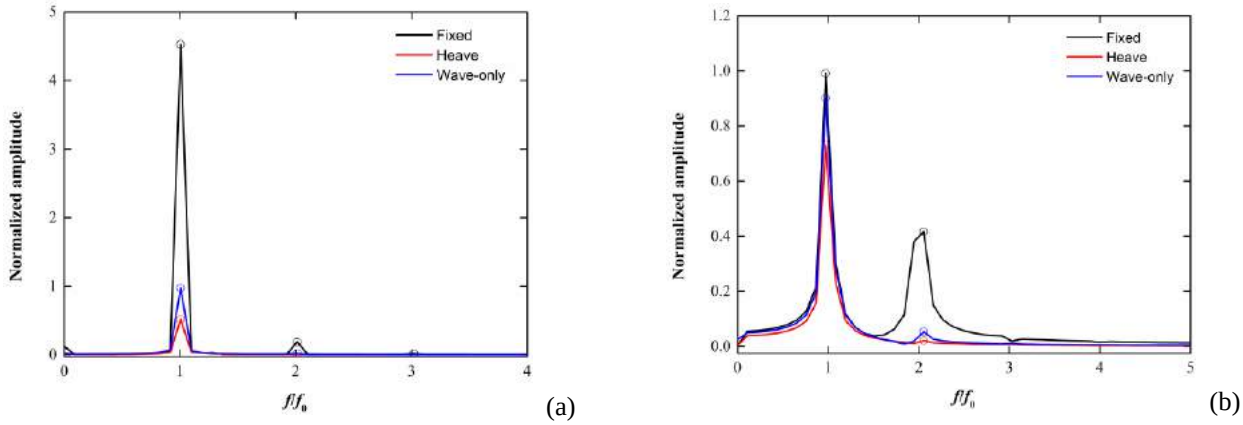

Figure 6: Normalized amplitude of the free surface elevation in the narrow gap for the *fixed system* and *heave system* under different incident wavelengths: (a) Stokes wave A (resonance); (b) Stokes wave B (half-resonance).

Table 1: Normalized harmonic components of wave elevation amplifications in the gap under different incident wavelengths

	$H_g^{(i)}/H_0$ ($H_g^{(i)}/H_g^{(1)}$)					
λ/h	i = 1		i = 2		i = 3	
	Fixed	Heave	Fixed	Heave	Fixed	Heave
4.044 (wave A)	4.53	0.258	0.19 (4.19%)	0.005 (1.94%)	0.02 (0.44%)	0.001 (0.39%)
	Fixed	Heave	Fixed	Heave	Fixed	Heave
9.920 (wave B)	0.991	0.731	0.42 (42.4%)	0.021 (2.87%)	0.03 (3.03%)	0.007 (0.96%)

Heave Displacements

Overall Displacements

The heave displacements of section B excited by the incident waves are monitored and analyzed to investigate the relationship between the heave motion and the gap resonance (see Figure 7). The non-dimensional vertical forces acting on section B are also displayed in the figure, where $A_0 = H_0/2$ denotes the incident wave amplitude. It is obvious that the heave displacement under the action of wave B is larger than that under wave A, while the vertical force is smaller. This is due to the fact that wave B is longer than wave A. A longer wave experiences less diffraction due to the presence of the upstream section, and thus more energy can be transmitted to the downstream to excite the motion of section B.

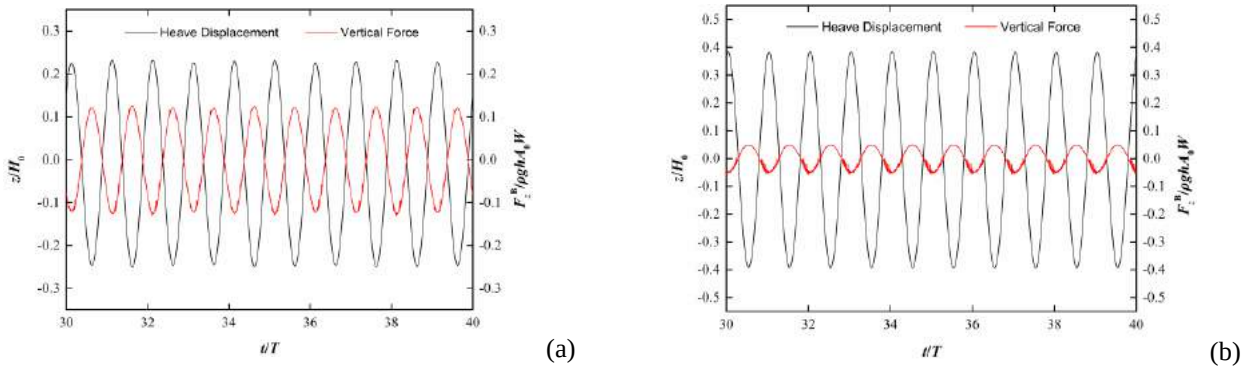

Figure 7: Time history of the heave displacement and the normalized vertical force of section B under different incident wavelengths: (a) Stokes wave A (resonance); (b) Stokes wave B (half-resonance).

Harmonic Analysis

The FFT method is also applied to the heave displacements of section B and the normalized amplitudes of first-, second- and third-harmonics are summarized in Table 2. It is noted that each harmonic of heave displacement is larger under wave B, which also indicates that more energy is transmitted from upstream to excite the heave motion. To link the harmonic components of the free-surface elevation in the gap with those of the heave displacement, the energy transmission alleviates the second-harmonic responses of the wave elevation within the gap for the incident wave B. In

general, the predicted motions of section B which is situated in the sheltered area of section A, are seen to be small. Intuitively, this is also a preferred ship-to-ship configuration in a practical bunkering operation.

Table 2: Normalized harmonic components of the heave displacements of section B under different incident wavelengths

	$Z^{(i)}/H_0$ ($Z^{(i)}/Z^{(1)}$)		
λ/h	$i = 1$	$i = 2$	$i = 3$
4.044 (wave A)	0.474	0.006 (1.29%)	0.002 (0.42%)
9.920 (wave B)	0.710	0.017 (2.25%)	0.004 (0.56%)

Flow Field Patterns

Additionally, the flow field near the sections for the *heave system* under the incident wave A is investigated to understand the viscous effect involved in the gap resonance. As illustrated in Figure 8, there is stronger vortex shedding at the upstream corners of the large fixed section. Obvious flow separation can be observed in the vicinity of the gap due to the violent piston-type motion of the fluid in the gap. However, the vorticity is much smaller than that for the *fixed system* with two identical sections owing to the sheltering from the upstream large section (details not shown here). Since the downstream section is allowed to move, it may have absorbed some of the energy from the fluid in the gap, which also appears to lead to a smaller liquid response in the gap. By examining the results of gap responses at resonances in Table 1, it seems that the heave motion has exhausted most of the energy accumulated by gap resonance.

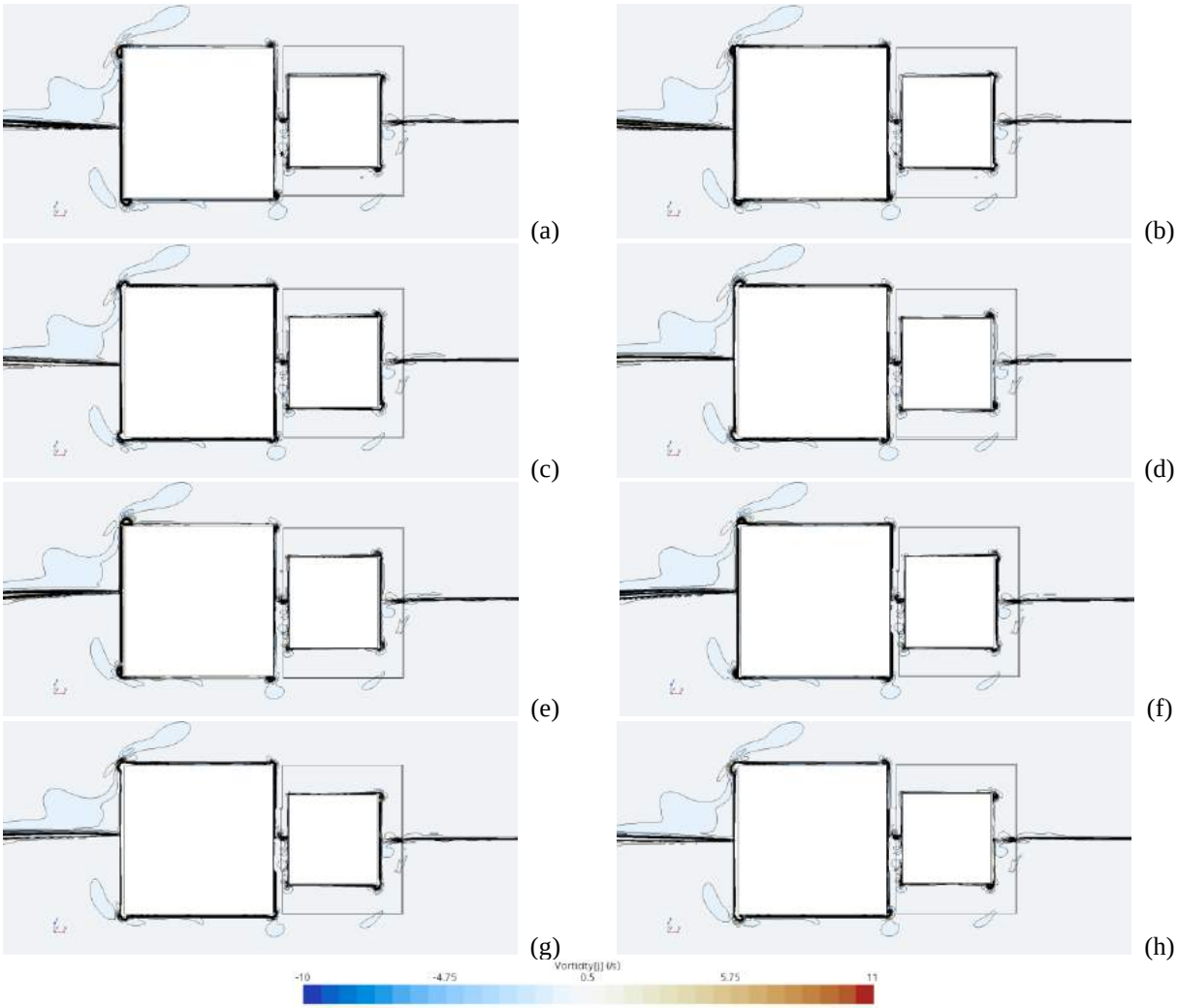

Figure 8: Vorticity contours near the sections during one period of heave motion in the narrow gap under the incident wave A: (a) 0*T*/8; (b) 1*T*/8; (c) 2*T*/8; (d) 3*T*/8; (e) 4*T*/8; (f) 5*T*/8; (g) 6*T*/8; (h) 7*T*/8.

CONCLUSIONS

A 2D numerical wave flume is established based on the URANS turbulence model and the VOF method to study the effect of the heave motion on the gap resonance between two non-identical rectangular cross-sections under different incident Stokes waves. The present work considers a more realistic scenario that a bunkering vessel, typically of smaller size, will hide behind a larger receiving vessel. The studied 2D cases are relevant for vessels under beam sea conditions. The free surface elevations inside the gap are compared between cases where the downstream section is either fixed or free to respond in heave. Harmonic components are analyzed to illuminate the frequency relation that incurs high-order resonance. The heave displacements are obtained and their harmonic components are also investigated to study the effect on the gap resonance. Some conclusions are drawn as follows:

(1) The first harmonics of the free surface elevation decrease with the wavelength for the *fixed system*, and large second harmonics are excited when the incident wave frequency is close to half the resonant frequency. The wave elevation in the gap for the *heave system* does not show a similar trend as that for the *fixed system*, which is due to the existence of the heave motion of the downstream section, thus leading to a modulation of free surface variation in the narrow gap and avoiding the second-order excitation.
(2) The heave motion under the action of a wave with a larger wavelength is more violent than that with a smaller wavelength. The vertical force acts like a resistance on the heaving section. Small force excited by the longer wave takes more energy from the water inside the gap and reduces the fluid response in the gap.
(3) As observed from the flow separation near both cross-sections, the sheltering effect achieved by hiding the small floating section behind the large fixed section can reduce the free surface elevation in the narrow gap and decrease the heave displacement to a large extent, which is a more preferred configuration for the bunkering operation at sea.

However, the bunkering operation can also be conducted in shallow water areas where Stokes wave theories are less applicable. Large free surface nonlinearity may also affect the gap response in the narrow gap. This part of the work is not included in the paper but will be presented during the conference.

ACKNOWLEDGEMENTS

This research was financially supported by China Scholarship Council (CSC No.202006060050) and performed using computational resources sponsored by Technical University of Denmark.

REFERENCES

CHUA, K. H., TAYLOR, R. E., and CHOO, Y. S. "Hydrodynamic interaction of side-by-side floating bodies part I: Development of CFD-based numerical analysis framework and modified potential flow model." *Ocean Engineering*, **166** (2018): 404-415.
FALTINSEN, O. M., FIROOZKOOHI, R., and TIMOKHA, A. N. "Steady-state liquid sloshing in a rectangular tank with a slat-type screen in the middle: Quasilinear modal analysis and experiments." *Physics of Fluids*, **23**:4 (2011): 042101.
FERZIGER, J. H., PERIĆ, M. *Computational methods for fluid dynamics*. Vol. 3. Berlin: springer, 2002.
GAO, J. L., et al. "Topographic effects on wave resonance in the narrow gap between fixed box and vertical wall." *Ocean Engineering*, **180** (2019): 97-107.
GAO, J. L., et al. "Numerical investigations of wave loads on fixed box in front of vertical wall with a narrow gap under wave actions." *Ocean Engineering*, **206** (2020): 107323.
GAO, J. L., et al. "Numerical investigations of gap resonance excited by focused transient wave groups." *Ocean Engineering*, **212** (2020): 107628.
GAO, J. L., et al. "Effects of free heave motion on wave resonance inside a narrow gap between two boxes under wave actions." *Ocean Engineering*, **224** (2021): 108753.
IWATA, H., SAITOH, T., and MIAO, G. P. "Fluid resonance in narrow gaps of very large floating structure composed of rectangular modules." *Proceedings of the fourth international conference on asian and pacific coasts*, Nanjing, China. 2007.
JIANG, S. C., BAI, W., and TANG, G. Q. "Numerical investigation of piston-modal wave resonance in the narrow gap formed by a box in front of a wall." *Physics of Fluids*, **31**:5 (2019): 052105.
JIANG, S. C., and BAI, W. "Coupling analysis for sway motion box with internal liquid sloshing under wave actions." *Physics of Fluids*, **32**:7 (2020): 072106.
JIANG, S. C., GU, Q., and CONG, P. W. "Fluid resonance in the narrow gap of a box-wall system under cnoidal wave action." *Ocean Engineering*, **238** (2021): 109774.
JIANG, S. C., BAI, W., and YAN, B. "Higher-order harmonic induced wave resonance for two side-by-side boxes in close proximity." *Physics of Fluids*, **33**:10 (2021): 102113.
KIM, J., O'SULLIVAN, J., and READ, A. "Ringing analysis of a vertical cylinder by euler overlay method." *International Conference on Offshore Mechanics and Arctic Engineering*. Vol. 44915. American Society of Mechanical Engineers, 2012.

KRISTIANSEN, T. and FALTINSEN, O. M. "Application of a vortex tracking method to the piston-like behaviour in a semi-entrained vertical gap." *Applied Ocean Research*, **30**:1 (2008): 1-16.
KRISTIANSEN, T. and FALTINSEN, O. M. "A two-dimensional numerical and experimental study of resonant coupled ship and piston-mode motion." *Applied Ocean Research*, **32**:2 (2010): 158-176.
LI, Y. J. and ZHANG, C. W. "Analysis of wave resonance in gap between two heaving barges." *Ocean Engineering*, **117** (2016): 210-220.
LI, Y. J. "Fully nonlinear analysis of second-order gap resonance between two floating barges." *Engineering Analysis with Boundary Elements*, **106** (2019): 1-19.
LU, L., et al. "Numerical investigation of fluid resonance in two narrow gaps of three identical rectangular structures." *Applied Ocean Research*, **32**:2 (2010): 177-190.
LU, L., et al. "Modelling of multi-bodies in close proximity under water waves—Fluid forces on floating bodies." *Ocean Engineering*, **38**:13 (2011): 1403-1416.
LU, L., et al. "Two-dimensional numerical study of gap resonance coupling with motions of floating body moored close to a bottom-mounted wall." *Physics of Fluids*, **32**:9 (2020): 092101.
MIAO, G. P. "Influence of gaps between multiple floating bodies on wave forces." *China Ocean Engineering*, **4** (2000): 407-422.
MOLIN, B. "On the piston and sloshing modes in moonpools." *Journal of Fluid Mechanics*, **430** (2001): 27-50.
MORADI, N., ZHOU, T. M., and CHENG, L. "Two-dimensional numerical study on the effect of water depth on resonance behaviour of the fluid trapped between two side-by-side bodies." *Applied Ocean Research*, **58** (2016): 218-231.
MUZAFERIJA, S. and PERIĆ, M. "Computation of Free Surface Flows using Interface Tracking and Interface Capturing Methods,'Chap. 2." *Mahrenholtz, O. and Markewicz, M., Nonlinear Water Wave Interaction, Comput. Mech. Publications* (1999).
NING, D. Z., et al. "Numerical study of resonance induced by wave action on multiple rectangular boxes with narrow gaps." *Acta Oceanologica Sinica*, **34**:5 (2015): 92-102.
NING, D. Z., et al. "Hydrodynamic difference of rectangular-box systems with and without narrow gaps." *Journal of Engineering Mechanics*, **141**:8 (2015): 04015023.
NING, D. Z., et al. "Experimental and numerical study on wave response at the gap between two barges of different draughts." *Applied Ocean Research*, **77** (2018): 14-25.
PERIĆ, M., and SWAN, C. "An experimental study of the wave excitation in the gap between two closely spaced bodies, with implications for LNG offloading." *Applied Ocean Research*, **51** (2015): 320-330.
PERIĆ, M. "Best practices for wave flow simulations." *The Naval Architect International Journal of the Royal Institute of Naval Architects* (2018).
RODRÍGUEZ, M. and SPINNEKEN, J. "A laboratory study on the loading and motion of a heaving box." Journal of Fluids and Structures, **64** (2016): 107-126.
SAITOH, T., MIAO, G. P., and ISHIDA, H. "Theoretical analysis on appearance condition of fluid resonance in a narrow gap between two modules of very large floating structure." *Proceedings of the 3rd Asia-Pacific Workshop on Marine Hydrodynamics*. China Ocean Press, 2006.
SUN, L., TAYLOR R. E., and TAYLOR, P. H. "First-and second-order analysis of resonant waves between adjacent barges." *Journal of Fluids and Structures*, **26**:6 (2010): 954-978.
TAN, L. et al. "Dissipative effects of resonant waves in confined space formed by floating box in front of vertical wall." *The Eleventh ISOPE Pacific/Asia Offshore Mechanics Symposium*. OnePetro, 2014.
TAN, L., et al. "A viscous damping model for piston mode resonance." *Journal of Fluid Mechanics*, **871** (2019): 510-533.
ZHAO, W. H., et al. "Estimation of gap resonance relevant to side-by-side offloading." *Ocean Engineering*, **153** (2018): 1-9.
ZHU, H. R., ZHU, R. C., and MIAO, G. P. "A time domain investigation on the hydrodynamic resonance phenomena of 3-D multiple floating structures." *Journal of Hydrodynamics*, **20**:5 (2008): 611-616.